Aluminum nanoparticle plasma formation for high-order harmonics generation

Aluminum nanoparticle plasma formation for high-order harmonics generation

Vyacheslav V. Kim,[1,2] Dmitry S. Ivanov,[3,4,5] Rashid A. Ganeev,[1,2,6,#] Mottamchetty Venkatesh,[1] Ganjaboy S. Boltaev,[1,2] Martin E. Garcia,[3] Baerbel Rethfeld,[4] and Chunlei Guo[1,7,*]

[1] The Guo China-US Photonics Laboratory, State Key Laboratory of Applied Optics, Changchun Institute of Optics, Fine Mechanics and Physics, Chinese Academy of Sciences, Changchun 130033, China
[2] Department of Physics, American University of Sharjah, PO Box 26666, Sharjah, UAE
[3] Theoretical Physics Department, University of Kassel, 34132 Kassel, Germany
[4] Technical University of Kaiserslautern and OPTIMAS Research Centre, 67663 Kaiserslautern, Germany
[5] Lebedev Physical Institute, 119991 Moscow, Russia
[6] Faculty of Physics, Voronezh State University, Voronezh 394006, Russia
[7] The Institute of Optics, University of Rochester, Rochester, NY 14627, USA
[#] rashid_ganeev@mail.ru * guo@optics.rochester.edu

Abstract. We demonstrate the efficient high-order harmonic generation (HHG) of 35 fs pulses from the nanoparticle (NP) – containing plasmas produced during laser ablation of aluminum target using picosecond and nanosecond pulses. The role of NPs in the enhancement of harmonic yield is discussed. To achieve the maximal HHG yield, we use different experimental schemes, including two-color pump, HHG using extended and multi-jet laser produced plasmas, ablation of rotating target, and temporal variation between the heating and driving pulses. A 5-fold increase of harmonic yield from Al NP-containing plasmas compared to the plasmas containing only aluminum atoms and ions is obtained. The harmonics up to the 35th order are generated from the Al NP-containing plasmas. HHG calculations show that this cutoff is attributed to Al neutral atoms rather than Al ions. To interpret the experimental results, we also study the fundamental mechanism of NP formation. The simulations are carried out for different Al NP-containing ablation plumes. Our calculations and plasma debris analysis show a presence of NPs in the plasmas exposing to the driving 35 fs pulses.
Keywords: laser-produced plasma; high-order harmonics; nanoparticles

1. Introduction

Laser-induced modification of surfaces using low fluencies of heating radiation allows the formation of direct nanoparticle and nanostructure formation [1,2]. Very first direct dynamic study and imaging of nanoparticle formation was reported in [3]. Additionally, laser induced ablation of surfaces at larger fluencies allows formation of the plasmas suitable for efficient generation of high-order harmonics during propagation of ultrashort pulses through the optimally formed plasma plumes [4]. The advantages of this method of coherent radiation generation in the extreme ultraviolet (XUV) range have been demonstrated in numerous studies, which showed the resonance-enhanced and quasi-phase matching-enhanced harmonics [5-17]. Further search of suitable laser-produced plasmas (LPPs) allows better understanding of the mechanisms of efficient high-order harmonics generation (HHG) in ionized media.

Aluminum plasma has some advantages due to the presence of small-sized nanoparticles (NPs) synthesized during ablation of solid target by laser pulses. Earlier, femto-, pico-, and nanosecond pulses were used for laser ablation to demonstrate the presence of NPs in LPPs [18,19]. The important issue is the stability of harmonic generation in NP-contained LPPs, which can be resolved using the method of the improvement of harmonic stability, when the target rotates during laser ablation [20,21].

To support the experimental data interpretation and to present a theoretical basis of the fundamental physical processes underlying the laser-induced formation of NPs, we perform a computer simulation of Al target evolution, followed by its excitation due to a single laser pulse. The simulation results are analyzed for investigation of the mechanism of NPs generation and their subsequent evolution during the expansion of the ablation plume, which will be then irradiated with the driving pulse for HHG. The analysis of laser ablation of Al in vacuum and the ablation plume dynamics can be performed using the combined atomistic-continuum model, the basics of which are described in [22]. The model is considering the kinetics of laser-induced phase transition processes at atomic level with the Molecular Dynamics (MD) approach [23], whereas the effect of free carriers in metals (absorption of the laser energy, fast electron heat conduction,

and non-equilibrium induced between elections and phonons) is addressed with the Two Temperature model (TTM) [24]. Such the combined MD-TTM model was already successfully used in our previous theoretical investigation on the investigation of the nanojet array structures formation on thin metallic films [25] and periodic patterning of metal targets with laser pulses on the experimental scale [26].

In this paper, we demonstrate the harmonic generation up to the thirties orders during propagation of 35 fs pulses through the aluminum plasma produced by either nanosecond or picosecond pulses. We show that the presence of strong ionic emission in the XUV range does not affects the yield of single nearby harmonic. The role of NPs in the enhancement of harmonic yield is discussed. Different schemes of laser-plasma interaction (two-color pump, harmonic generation in extended and multi-jet LPP, ablation of rotating target, temporal variation between heating and driving pulses, etc.) are demonstrated. Our calculations and plasma debris analysis demonstrate the presence of NPs in the plasmas during propagation of driving pulses.

2. Experimental studies of HHG in Al LPP

2.1. Experimental arrangements

Femtosecond laser radiation (800 nm, 35 fs, 1 kHz; Spectra Physics, Spitfire Ace) was focused using a 400-mm focal length spherical lens in the vacuum chamber (Fig. 1). The maximal used intensity of 800 nm femtosecond pulses in the focal plane was 5×10^{14} W cm^{-2}. Most of experiments were carried out using the single-color pump (SCP) of LPP. To generate harmonics using two-color pump (TCP), the barium borate (BBO) crystal was inserted in the vacuum chamber on the path of the focused 800 nm radiation to generate 400 nm radiation. The 5-mm long plasma plume was produced by 200 ps, 800 nm pulses focused by cylindrical lens. The ablation of target was also carried out by nanosecond laser pulses (1064 nm, 5 ns, 10 Hz; Coherent, Q-Smart) and femtosecond laser pulses (800 nm, 35 fs, 1 kHz).

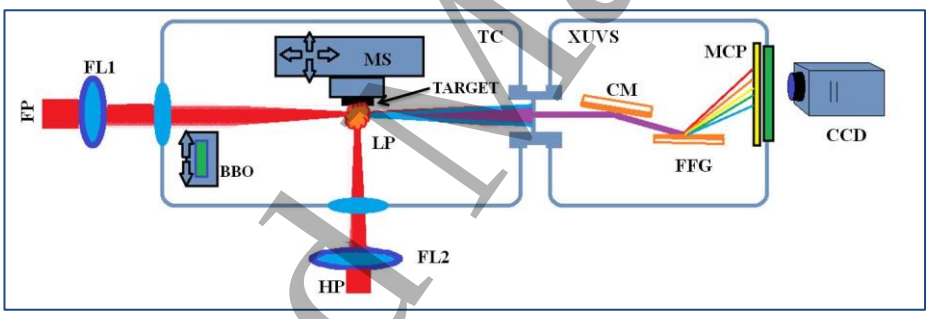

Fig. 1. Experimental setup for high-order harmonic generation in aluminum plasma. TC, target chamber; XUVS, extreme ultraviolet spectrometer; FP, femtosecond pulse; FL1 and FL2, focusing lenses; MS, motion stage; BBO, barium borate crystal; HP, heating pulse; LP, laser produced plasma; CM, cylindrical mirror; FFG, flat field grating; MCP, micro-channel plate; CCD, CCD camera.

In present studies, the highest harmonic yield from Al LPP was obtained at ~70 - 100 ns from the beginning of target ablation. The plasma concentration was estimated to be 3×10^{17} cm^{-3}. XUV spectrometer was used for analysis of harmonic emission.

The formation of quasi-phase matching (QPM) conditions for driving and harmonic waves in LPPs was analyzed by variation of the morphology of extended LPPs using spatially structured heating beams. To create heterogeneous spatial heating of targets we used the multi-slit masks (MSM) installed in front of the targets, which allowed formation of the multi-jet plasmas (MJP) containing different number of jets depending on the number of slits in the MSM.

Aluminum was used as the target with the sizes of $5\times5\times1$ mm^3 for ablation and formation of LPPs. We also used the rotating Al rod for stabilization of harmonic yield produced at 1 kHz pulse repetition rate.

2.2. Harmonic generation in aluminum plasma

Analysis of plasma debris was accomplished using the scanning electron microscope (SEM).

Figures 2(a,b) show SEM images in the cases of ablation by picosecond and femtosecond pulses. Notice that both femtosecond, picosecond and nanosecond pulses allowed formation of NPs during laser ablation. The mean sizes of NPs in the two latter cases were 35 nm (during ablation by picosecond pulses; inset in Fig. 2c) and 20 nm (during ablation by 5 ns pulses).

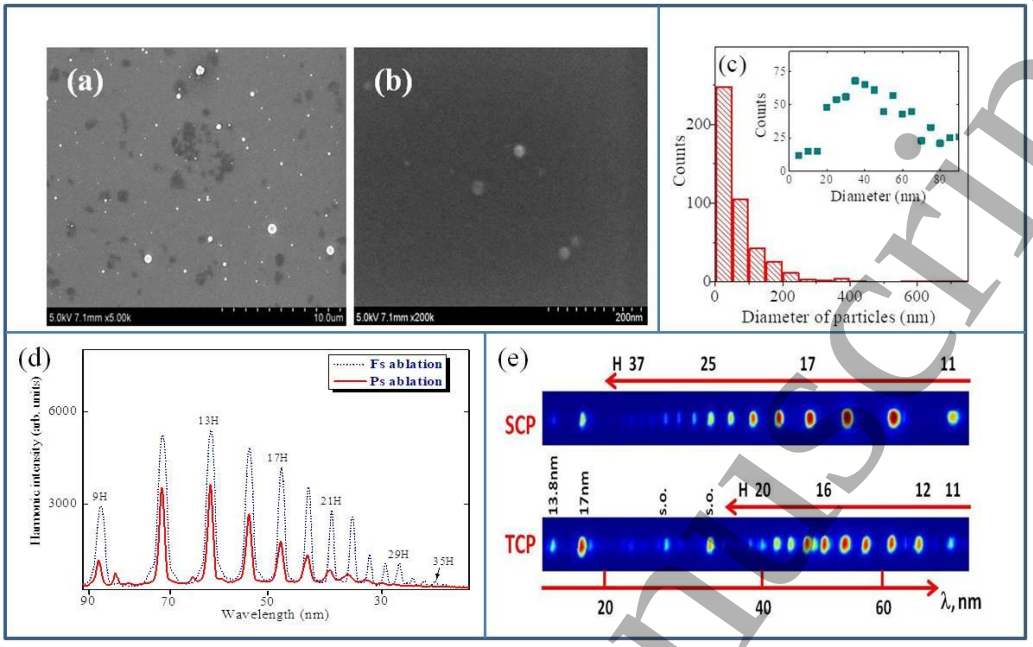

Fig. 2. (a) SEM images of deposited Al NPs during ablation by picosecond pulses. (b) SEM images of deposited Al NPs during ablation by femtosecond pulses. (c) Histogram of Al NPs produced during ablation by femtosecond pulses. Inset: Histogram of Al NPs produced during ablation by picosecond pulses. (d) Harmonic spectra from the Al plasma produced by femtosecond (dotted curve) and picosecond (solid curve) pulses. (e) Images of harmonic spectra from Al LPP in the cases of SCP (upper panel) and TCP (bottom panel). Here we also show Al III emission lines (13.8 and 17 nm) and its second orders (s.o.).

Aluminum plasma has already been studied as the medium for harmonics emission [27]. Those studies have revealed some uncertainties in determination of the impeding processes occurring during propagation of femtosecond pulses through Al LPP. Here we present the detailed experimental analysis of HHG in aluminum plasma assuming the influence of NPs appearing in *situ* during ablation of solid target.

Ablation using pulses of different duration may distinguish the most suitable regimes of plasma formation for HHG. We carried out the femtosecond- and picosecond-pulses induced ablation of aluminum for analysis of HHG efficiency in Al plasma. Figure 2d shows two spectra of harmonics generated in the plasmas produced by femtosecond (solid curve) and picosecond (dotted curve) pulses on the aluminum target. These studies showed the preferences in application of short laser pulses for formation of suitable plasma for HHG. The cutoff of harmonics in that case was notably larger (H35) compared with the ablation by picosecond pulses (H27). The conversion efficiency in the former case was also higher than in the latter case.

To address the observed harmonic cutoff in aluminum plasma we used the Lewenstein model of HHG [28]. Al and Al^+ were modeled using simple hydrogen-like model. First and second ionization potentials were taken equal to 5.98 eV and 18.83 eV. The results of our calculations are presented in Fig. 3. The positions of cutoff for each spectra were estimated using the expression from [29], where the cutoff was equal to the integer part of $(I_p+3.2U_p)/\omega$ (I_p is the potential of ionization, U_p is the quiver energy of electron and ω is the frequency of laser). The evaluation of barrier suppression intensity [30] gives us $I_{BSI}=2.6\times10^{13}$ W cm^{-2} for the first and $I_{BSI}=2.7\times10^{15}$ W cm^{-2} for the second ionization potentials.

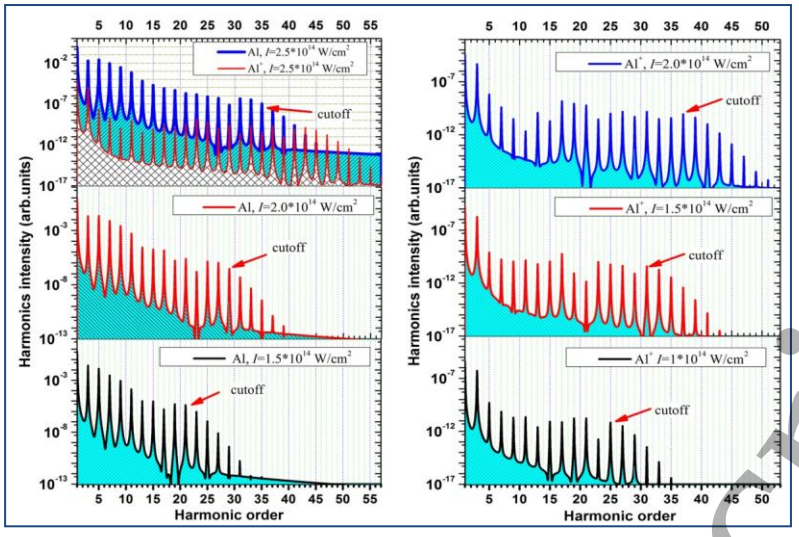

Fig. 3. Calculated harmonic spectra for Al (left panel) and Al^+ ion (right panel).

Our simplified model demonstrates some mismatch in the value of laser field intensity I in focal spot. According to calculations, HHG spectra achieve the H35 cutoff at $I \approx 2.5\times10^{14}$ W cm^{-2} for neutral Al atoms and at $I \approx 2\times10^{14}$ W cm^{-2} for Al^+. The difference between experiment ($I \approx 3.5\times10^{14}$ W cm^{-2}) and theory can be partially explained by the uncertainty of the experimental measurements of laser intensity. Although presence of positively charged ions is confirmed by observation of the plasma emission, Lewenstein model predicts sufficiently lower conversion efficiency for Al^+ ions. On the top left panel of Fig. 3 we show two HHG spectra from Al and Al^+ at laser intensity $I \approx 2.5\times10^{14}$ W cm^{-2}, one can compare the conversion efficiencies from two components of plasma, which is sufficiently lower in the case of Al^+ at the middle of HHG plateau and 2 orders of magnitude less in the cutoff region.

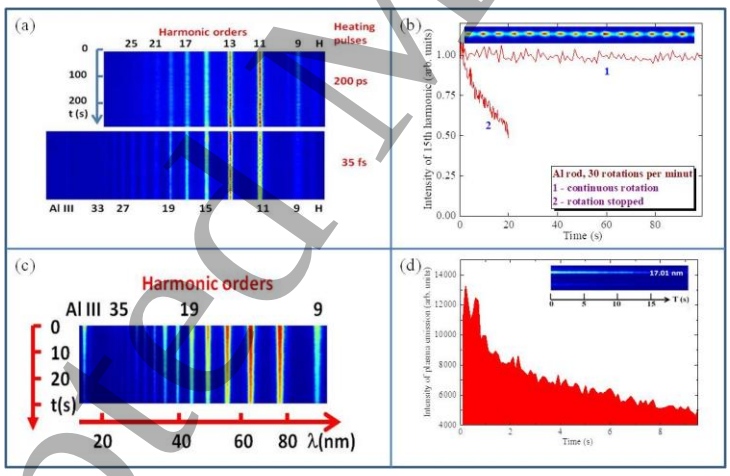

Fig. 4. Stability measurements of the plasma and harmonic spectra from the plasma produced on the rotating aluminum rod. (a) Combined images of HHG spectra collected during 5 min. Upper and bottom panels of spectra correspond to the heating of Al rod by 200 ps and 35 fs pulses respectively. (b) Time-dependent variation of the intensity of the 15th harmonic generating from the aluminum plasma produced by picosecond pulses. Curve 1 corresponds to constant rotation of Al rod and curve 2 corresponds to the abrupt termination of rotation. Inset: snapshots of 15 pulses of H15 collected during 1.5 seconds of ablation of the rotating aluminum rod. (c) Decay of plasma emission (17.01 nm, Al III) and harmonics after abrupt stopping of rotation rod at the moment corresponding to 0 s. (d) Decrease of 17.01 nm emission excited by 35 fs pulses during ablation of stopped Al target. Inset: Image of the part of XUV spectrum showing the decay of 17.01 nm emission line of Al III excited by 200 ps pulses after stopping the rotation of ablating rod.

We also carried out HHG using the two-color (TCP, 800 nm + 400 nm) pump of aluminum plasma. TCP was studied earlier in both gases and plasmas [31-36]. Figure 2e shows the images of harmonic spectra from Al NP plasma produced by femtosecond pulses in the cases of SCP (upper panel) and TCP (bottom panel). We observed even harmonics up the 20th order. One can see the approximately similar intensities of odd and even harmonics until the harmonic cutoff (H19). Here we also identified the Al III emission lines (13.8 and 17 nm) and their second orders. The growth of heating picosecond pulse intensity above 2×10^{10} W cm^{-2} led to a considerable decrease of harmonic yield. The high-order harmonics disappeared at higher energies of heating radiation. The ablation of Al target using the heating pulse fluence above a certain level led to the appearance of multiply charged ions and strong plasma emission.

During most of studies, we used the uncompressed 200 ps pulses from the same laser, which provided the driving laser pulses, as the heating radiation, alongside the 5 ns pulses from another laser. Meanwhile, the application of 35 fs pulses as the heating radiation allowed the extension of harmonic cutoff up to the 35th harmonic (54.2 eV, Fig. 4a). This figure shows the images of stable harmonics generation during ablation of the rotating Al rod.

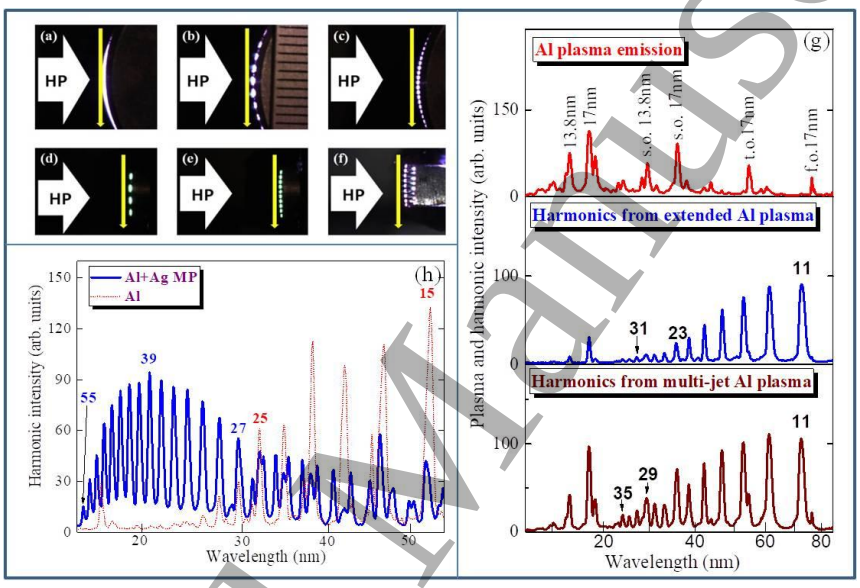

Fig. 5. (a-f) Schemes for formation of (a) extended plasma, and (b,c) MJP using different MSMs containing 0.5 and 0.2 mm slits in the case of rotating Al rod. Yellow arrows correspond to the direction of driving femtosecond pulse propagation. Similar MJPs in the case of the plane surface of aluminum target are shown in (d) and (e). (f) Formation of two groups of MJPs on the top and bottom of the perforated Al target. Bottom plasma does not participate in interaction with the driving femtosecond pulses due to delayed appearance of this group of plasma jets on the path of laser pulses. (g) Plasma (upper panel) and harmonic (two bottom panels) spectra from Al plasma. Middle and bottom panels correspond to the extended (5-mm) homogeneous plasma and multi-jet plasma (10 jets of 0.2 mm length each; corresponds to the image shown in (e)). One can see the enhancement of highest orders in the latter case. (h) Harmonic spectra in the case of perforated Al target (dotted curve; corresponds to the plasma image shown in (f) and the same target filled with the Ag microparticles inside the empty parts of Al target (solid curve).

Our studies showed that stable harmonic emission in the case of rotating target (Fig. 4b, curve 1) was significantly worsened once the rotation stopped (see the curve 2 of Fig. 4b). The same can be said about the emission lines of Al in the shorter-wavelength range. Figures 4c and 4d show the decay in the plasma emission at the wavelength of the Al III transition excited by femtosecond pulses. After ten seconds from stopping the rotation of Al rod the intensity of 17.01 nm line decreased by almost three times (Fig. 4c). The same was observed in the case of ablation by picosecond pulses. Inset in Fig. 4d shows the raw image of Al III plasma line at the wavelength of 17.01 nm excited using 200 ps, 800 nm heating pulses.

The application of MJP instead of the extended imperforated plasma formations have earlier shown the group of enhanced harmonics [37,38], similarly to the case of the multi-jet gases [39,40]. Here we demonstrate the application of heterogeneous aluminum MJP for generation of the groups of enhanced harmonics at different configurations of experiments. The schemes for formation of the groups of separated plasma jets are depicted in Fig. 5(a-f). The application of rotating target presents a new approach in realization of QPM during harmonic generation in heterogeneous aluminium plasma jets excited on the surface of Al rod. The diameter of Al rod was equal to 25 mm. The realized approach allowed the formation of the heterogeneous plasma plumes on the rounded surfaces (Fig. 5(b,c)). The plasma particles from different parts of ablated rounded surface of the rod were delayed from each other due to different distances from the surface to the axis of femtosecond beam propagation. The main conception of the QPM at these conditions is a formation of the difference between the phases of driving pulses and some generated harmonics based on the optical dispersion of plasma jets.

Figures 5(a-f) show the plasmas formed on the surfaces of Al rod, plane Al plate, and perforated Al target using the cylindrical focusing lens. Ablation of rotating aluminum target by the radiation focused using cylindrical lens caused the formation of the extended plasma on the rotating target (Fig. 5a). Once we installed the MSMs with the slit sizes of 0.5 (Fig. 5b) and 0.2 mm (Fig. 5c), the corresponding variation of the shape of plasma from extended one to the MJP was performed. Ablation by similar heating pulses propagating through different MSMs led to the variation of the shape of the MJP formed on the ablating surface (Figs. 5d and 5e). Finally, we show the irradiation of perforated aluminum target (Fig. 5f), when plasma became periodically formed on the tops and bottoms of the sample. Notice that the plasma formed on the bottom sides of target did not participated in harmonics generation due to longer path propagation until the interaction with the driving femtosecond pulses.

Our attempts to generate the QPM-enhanced harmonics in the shorter wavelength range in the case of perforated Al target (Fig. 5f) did not reveal the growth of those harmonics. Figure 5g (two bottom curves) shows the featureless decrease of harmonic yield for each harmonic order. Meanwhile, the insertion of silver microparticles in the empty areas of the Al target (Fig. 5f) led to their ablation and formation of the QPM-enhanced group of shorter-wavelength harmonics centered at H39 (Fig. 5h, thick solid curve; compare with thin dotted curve corresponding to the perforated Al target).

The presence of strong ionic emission in XUV range did not affect the yield of single nearby harmonic, which points out the absence of the influence of ionic transitions on the harmonic efficiency, probably due to small oscillator strength of those transitions. The emission from plasma did not exceed the harmonic emission, since we avoided the formation of highly excited plasmas.

We suppose that laser-produced plume from the surface of aluminum target at optimal fluence of heating pulses mostly consisted of neutral atoms and small amount of Al ions. Correspondingly, after passing of the pulse with intensity of 2.5×10^{14} W cm^{-2} most of particles became ionized. Meanwhile, according to Lewenstein's model, the emission with highest contribution to HHG spectra corresponds to the trajectories with 0.65T return time (where T is the period of a single cycle of the laser field), so generally speaking two cycles are enough to generate the whole HHG spectrum up to the cutoff region. One has to calculate the saturation intensity for our 35 fs pulses, which correspond to approximately 13 cycles, to assure that all ionization happens at the leading part of pulse.

In present experiments, the measured ratio of harmonic yields from ablated Al NPs and bulk aluminum targets was 5:1. We did not carry out the comparative studies of the harmonic fluxes from Al NPs and argon gas. Meantime, recent studies of the comparative efficiencies of HHG in Ar gas and different metal plasmas [41] have demonstrated the stronger harmonic yield from Ag, Ag_2S, and stainless steel LPPs than the one generated from argon gas. A three- to twenty-fold increase of harmonic yield was found from those LPPs compared to the gas medium under similar experimental conditions. Meantime, the studies of the efficiencies of HHG from ablated Al NPs and bulk silver targets carried out in separate experiments were estimated to be at the ratio of 3:1,

thus giving us the approximate absolute value of conversion efficiency from aluminum NPs (2.5×10^{-5}) taking into account the earlier reported HHG conversion efficiency in Ag atoms and ions contained LPP (8×10^{-6}, [42]). One can deduce from above measurements and calculations that the conversion efficiency of harmonic generation from Al NPs should be larger than from argon gas. Thus NP targets can be considered as an alternative to pure atomic gas jets provided the amendment and progress in the technical issues for the formation of stable nanoparticle-contained LPPs.

Stronger harmonic flux from NPs with regard to the monomers could be attributed to better conditions of the formation of harmonic emitters in the case of Al NP formation and spreading, as well as to specific properties of NPs [43-49], which include the ionization and recombination to the same ion of cluster, to the neighboring ions and to the whole cluster. In [50], the general physics of HHG in the plasmas containing small-sized nanoparticles has been discussed based on the advanced properties of these nanostructures compared with the plasmas containing atoms and ions. The theoretical justification of utilizing the plasmonic fields in gold nanoparticles for the generation of efficient coherent XUV radiation has been reported in [51]. The HHG process in the presence of such structures can be explained by the higher nonlinear optical response of materials based on the plasmonic properties of NPs and quantum dots. Plasmon-enhanced high-harmonic generation from silicon was reported in [52]. The authors proposed that the field can become strong enough to convert the fundamental laser frequency into high-order harmonics through an extremely nonlinear interaction with gas atoms that occupy the nanoscopic volume surrounding the nanoantennas.

3. Theoretical analysis of nanoparticles formation in vacuum during ablation of aluminum by 50 ps pulses

3.1. Basic principles

In order to advance in understanding of the fundamental physical processes underlying the laser-induced formation of NPs we performed a computer modeling of ablation by picosecond pulses of the thick aluminum target at the incident fluence of 10 J cm^{-2}. This fluence was used during the laser ablation of aluminum by 200 ps pulses. The pulse duration of 50 ps is chosen since it much larger than the characteristic electron-phonon equilibration time for Al (~1.5 ps) [53], so that it allows us to keep the efficiency of calculation high enough, but the obtained results should be similar within the pulse range of hundreds of picoseconds. Thus, in order to get a general scope on the mechanisms responsible for the NPs generation process, we simulate the Al target evolution, followed by an interaction with 50 ps pulse at the wavelength of 800 nm and at the incident fluence of 10 J/cm^2 focused into 0.3 mm laser spot at the material surface.

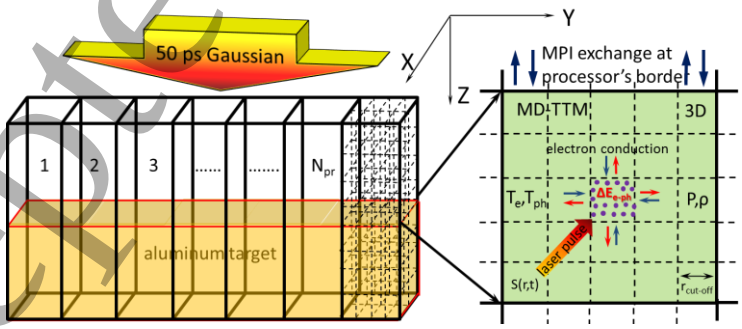

Fig. 6. Computational box for simulations of laser-induced formation of NPs is divided into the number of subsells N_x and N_y in X and Y directions correspondingly to be processed by N_x*N_y processor' cores (left). Each separate core is divided to 3D mesh and shown in 2D view (right). The laser beam of 0.3 mm in diameter is focused along Z axis.

The computational cell used in the simulation of the NPs formation process is schematically shown in Fig. 6. The laser spot size focused on the metal surface (0.3 mm) can be considered as

large enough as compared to the lateral size of the simulating volume (100 nm). This assumes a uniform laser intensity distribution across the surface within the computational box and justifies the Periodic Boundary Conditions (PBC) in X and Y directions during our simulation time of 500 ps. The lateral dimensions of the computational box must also suit the demands on the identical comparison of the modeling results and the experiment data. Thus, the total computational cell must accommodate the generated nanoparticles, the size of which (based on the experimental data) can be estimated in the range of ~ 10-50 nm.

The computational cell, consisting of ~45,000,000 atoms, was generated with the dimensions of 75×100×400 nm in X, Y, and Z directions respectively. Unnecessary and expensive MD integrations in the deep bulk of material, where no phase transitions or any crystal structure changes are induced, can be skipped by means of imposing the Non Reflective Boundary (NRB) conditions at the depth of 400 nm from the surface [54]. Thus, the combined MD-TTM model was applied only above that limit and the only TTM model was solved beneath the NRB, accounting for the electron-phonon temperature dynamics on a scale up to 50 μm from the surface [55].

For a possibility of the direct comparison of the simulation results with the experimental data, a realistic interatomic potential for Al was implemented in MD-TTM model [24]. This potential reproduces the thermophysical properties of Al (melting temperature, heat capacity, volume of melting, and linear thermal expansion coefficient) with an accuracy of more than 99.5% [56]. At last, the values of incident and absorbed fluencies were related through the reflectivity function of aluminum, R = 0.87, in accordance with the tabulated values of extinction coefficients [57] at the wavelength of 800 nm.

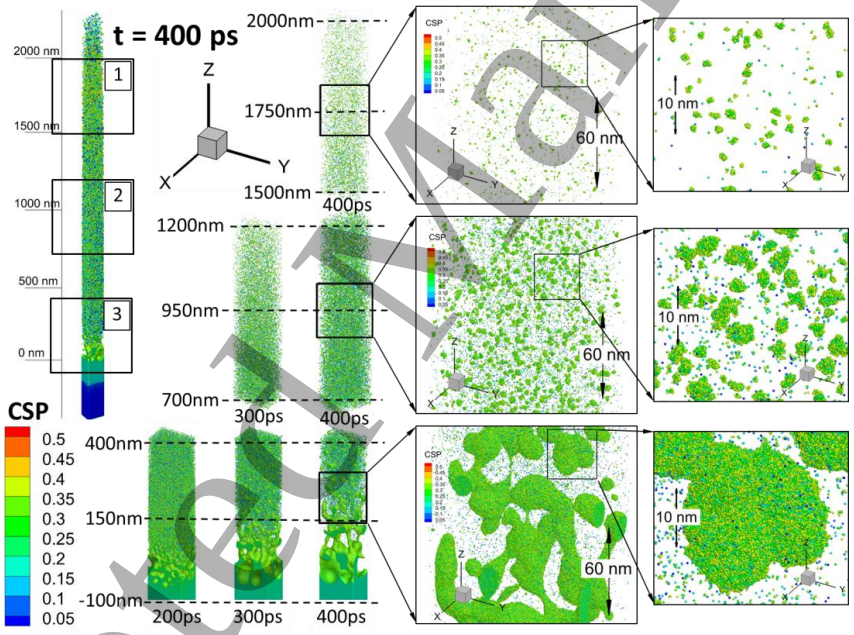

Fig. 7. The atomic snapshots are shown for a visual analysis of NPs formation using the 50 ps laser pulse interacting with a thick Al in vacuum target at the incident fluence of 10 J cm^{-2}. The general view of the process is caught at the time of 400 ps on the left. Three different areas of the ablation process are additionally shown as sequences of the corresponding snapshots for the squares “1”, “2”, and “3”. The atoms are colored by Central Symmetry Parameter (SCP) for identification of the crystal structures as follow: solid < 0.08 < defects < 0.12 < liquid < 0.25 < surface < 0.50 < vapor. The final stages for all three areas are additionally zoomed on the right for a more a closer view and additionally zoomed for the detailed investigation of the NPs’ shape and size.

3.2. Results of modeling and discussion

The results of modeling of NPs formation due to a 50 ps laser pulse interacting with a thick Al target are shown in Fig. 7, where by the time of 400 ps one can identify three essential zones for the NPs formation. For each of the zones (“1”, “2”, and “3”) we show the sequence of 3D atomic snapshots at the selected times of 200 ps, 300 ps, and 400 ps from the begging of simulation, Fig.

8. Gaussian pulse reaches its maximum at the time of 125 ps (we take $5\tau_{pulse}$ to inscribe the Gaussian pulse).

The laser pulse, being much longer than the characteristic electron-phonon relaxation time, cannot induce strong electron-phonon non-equilibrium. The electronic temperature therefore, does not reach high values and becomes limited roughly within 10,000 K, when the laser deposited energy dissipation channel through the electron heat conduction is much weaker than the energy dissipated through the electron-phonon collisions (lattice heating) [58]. This results in the establishment of thermal confinement regime and the incurred damage therefore has purely thermal character [59]. Nevertheless, during the laser energy deposition, the long heating time results in reaching the critical temperature value of more than 6000 K for the lattice and the ablation process is driven by the explosive boiling mechanism [54].

From the snap shots (200ps, 300ps, or 400ps), shown for each of the zones in Fig. 7, one can observe the evolution of Al target's atomic structure in the corresponding zones. The atoms are colored by Central Symmetry Parameter (CSP) for identification of their local structure: solid < 0.08 < defects < 0.12 < liquid < 0.25 < surface < 0.50 < vapor. The final stages of each of the regions are zoomed for the detailed visual investigation of the forming particle sizes and spatial distribution. They are additionally zoomed to observe their shape and local structure. The top zone "1" contains the smallest Al NPs with rather spherical shape and the characteristic size of ~ 1-2 nm. The zone "2" has the particles of rougher form, but of bigger size ~ 4-5 nm. And finally, the area "3" shows the part of the material, where the formation of the NPs is still in progress due to the ablation mechanism, where the forming droplets have the characteristic size of ~ 30-40 nm.

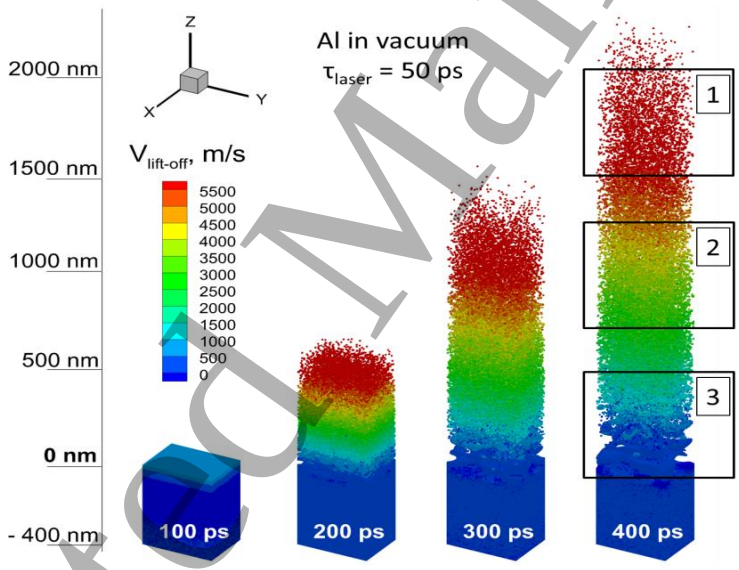

Fig. 8. The lift-off velocity fields of the material ejection process is shown by color in the sequence of the contour snapshots for the selected times of 100, 200, 300, and 400 ps. The last snapshot reveals the relative position of the zones "1", "2", and "3" with respect to each other as they introduced in the description of Fig. 7.

Since the material ejection process is governed by the explosive boiling mechanism, the initially heated sample is undergone to the intensive boiling and evaporation process, which is reflected in the region "1", where the fastest atoms form the smallest nanoparticles, moving with the speed of ~ 6500 m s^{-1}. This can be seen in Fig. 3, where we show the sequence of the contour snapshots for the lift-off velocity fields of the ejected material. Meantime the intensive evaporation process efficiently cools down the surface due to the transfer of thermal energy into the enthalpy of vaporization. Thus, the NPs with the lower kinetic energy, but with large size form the region "2", which moves at a slower speed of ~ 3500 m s^{-1}. Finally, when the material's surface loses most of its thermal energy, we observe the ordinary material ejection process due to

rather spallation mechanism [60]. During the spallation process the liquid material is ejected in large chunks due to initially obtained kinetic energy, forming therefore the region "3" with the characteristic size of the NPs of ~30 nm and moving roughly at the speed of ~ 750 m s^{-1}.

Further evolution of the ablation plume will result in a more pronounced segregation of the formed NPs, as they are presented in "1", "2", and "3" zones, in accordance with their size and the lift-off velocity. Their solidification process will take place on a much longer time scale and will be governed by the surrounding media. Thus, knowing the delay between the heating and the driving pulses, and the distance from the initial material's surface for the driving pulse shot one can select the specific size and spatial distribution of the formed NPs for the subsequent HHG process.

4. Conclusions

In conclusion, we have demonstrated the harmonics generation up to the thirties orders during propagation of 35 fs pulses through the aluminum plasma produced by either nanosecond or picosecond and femtosecond pulses. We have shown that the presence of strong ionic emission lines in the XUV range does not affects the yield of single nearby harmonics. The role of NPs in the enhancement of harmonic yield is discussed. We have shown a 5-fold growth of harmonic yield of harmonics in the case of Al NP plasma compared with the plasmas generally containing the Al atoms and ions. We have applied different schemes of laser-NP-plasma interaction in the case of ablated aluminum target (two-color pump, harmonic generation in extended and multi-jet LPP, ablation of rotating target, temporal variation between heating and driving pulses, etc.). Harmonics up to the 35^{th} order were obtained in the case of the formation of NP plasma using the femtosecond pulses. Our calculations have shown that this cutoff is attributed to the involvement of Al neutral atoms rather than Al^+.

Our calculations and plasma debris analysis have demonstrated the presence of NPs in the plasmas during propagation of driving pulses. The performed MD-based simulation of the laser pulse interaction with aluminum target allowed extracting the mechanism of the NPs formation. The simulation results showed that the NPs in the expanding ablation plume segregate by the size due to obtained lift-off speed. This segregation, therefore, can be used for selective NPs' size irradiation with the driving pulse, which assumes the controlled HHG process by manipulating with the delay between the heating and driving pulses.

Funding. National Key Research and Development Program of China (2017YFB1104700, 2018YFB1107202), National Natural Science Foundation of China (NSFC, 91750205, 61774155, 61705227), Bill & Melinda Gates Foundation of the US (OPP1157723), Scientific Research Project of the Chinese Academy of Sciences (QYZDB-SSW-SYS038), Jilin Provincial Science & Technology Development Project (20180414019GH), The Key Program of the International Partnership Program of CAS (181722KYSB20160015). Chinese Academy of Sciences President's International Fellowship Initiative (PIFI, 2018VSA0001), German Science Foundation (DFG IV 122/4-1, GA 465/15-2).

Acknowledgments. The MD simulations were performed at Lichtenberg Super Computer Facility TU-Darmstadt (Germany).National Key Research and Development Program of China (2018YFB1107202, 2017YFB1104700), National Natural Science Foundation of China (NSFC, 91750205, 61774155, 61705227), K.C.Wong Education Foundation (GJTD-2018-08), Scientific Research Project of the Chinese Academy of Sciences (QYZDB-SSW-SYS038), Jilin Provincial Science & Technology Development Project (20180414019GH), The Key Program of the International Partnership Program of CAS (181722KYSB20160015).

References

1. A.Y. Vorobyev and C. Guo, Opt. Express 14, 2164 (2006).
2. A.Y. Vorobyev and C. Guo, Laser Photon. Rev. 7, 385 (2013).
3. R. Fang, A. Y. Vorobyev, and C. Guo, Light Sci. Appl. 6, e16256 (2017).
4. R. A. Ganeev, *High-Order Harmonic Generation in Laser Plasma Plumes*, Imperial College Press (2012).

5. R. A. Ganeev, V. I. Redkorechev, and T. Usmanov, Opt. Commun. 135, 251 (1997).
6. R. A. Ganeev. Frequency Conversion of Ultrashort Pulses in Extended Laser-Produced Plasmas, Springer Science and Business Media LLC (2016).
7. H. Singhal, V. Arora, B. S. Rao, P. A. Naik, U. Chakravarty, R. A. Khan, and P. D. Gupta, Phys. Rev. A 79, 023807 (2009).
8. Y. Pertot, L. B. Elouga Bom, V. R. Bhardwaj, and T. Ozaki, Appl. Phys. Lett. 98, 101104 (2011).
9. L. B. Elouga Bom, Y. Pertot, V. R. Bhardwaj, and T. Ozaki, Opt. Express 19, 3677 (2011).
10. Y. Pertot, S. Chen, S. D. Khan, L. B. Elouga Bom, T. Ozaki and Z. Chang, J. Phys. B: At. Mol. Opt. Phys. 45, 074017 (2012).
11. S. Haessler, V. Strelkov, L. B. Elouga Bom, M. Khokhlova, O. Gobert, J.-F. Hergott, F. Lepetit, M. Perdrix, T. Ozaki, and P. Salières, New J. Phys. 15, 013051 (2013).
12. N. Rosenthal and G. Marcus, Phys. Rev. Lett. 115, 133901 (2015).
13. A.S. Emelina, M. Y. Emelin, R. A. Ganeev, M. Suzuki, H. Kuroda, and V. V. Strelkov, Opt. Express 24, 13971 (2016).
14. M. A. Fareed, V. V. Strelkov, N. Thiré, S. Mondal, B. E. Schmidt, F. Légaré, and T. Ozaki, Nature Commun. 8, 16061 (2017).
15. M. Wöstmann, L. Splitthoff, and H. Zacharias, Opt. Express 2018, 26, 14524.
16. Z. Abdelrahman, M. A. Khohlova, D. J. Walke, T. Witting, A. Zair, V. V. Strelkov, J. P. Marangos, and J. W. G. Tisch, Opt. Express 26, 15745 (2018).
17. M. A. Fareed, V. V. Strelkov, M. Singh, N. Thiré, S. Mondal, B. E. Schmidt, F. Légaré, and T. Ozaki, Phys. Rev. Lett. 121, 023201 (2018).
18. A.A. Ionin, S. I. Kudryashov, S. V. Makarov, L. V. Seleznev, and D. V. Sinitsyn, Appl. Phys. A 117, 1757 (2014).
19. E. G. Gamaly, N. R. Madsen, M. Duering, A. V. Rode, V. Z. Kolev, and B. Luther-Davies, Phys. Rev. B 71, 174405 (2005).
20. C. Hutchison, R. A. Ganeev, T. Witting, F. Frank, W. A. Okell, J. W. G. Tisch, and J. P. Marangos, Opt. Lett. 37, 2064 (2012).
21. R. A. Ganeev, J. Zheng, M. Wöstmann, H. Witte, P. V. Redkin, and H. Zacharias, Eur. Phys. J. D 68, 325 (2014).
22. D. S. Ivanov, A. I. Kuznetsov, V. P. Lipp, B. Rethfeld, B. N. Chichkov, M. E. Garcia, and W. Schulz, Appl. Phys. A 111, 675 (2013).
23. D. S. Ivanov, A. Blumenstein, J. Ihlemann, P. Simon, M. E. Garcia, and B. Rethfeld, Appl. Phys. A 123, 744 (2017).
24. V. V. Zhakhovskii, N. A. Inogamov, Y. V. Petrov, S. I. Ashitkov, and K. Nishihara, Appl. Surf. Sci. 255, 9592 (2009).
25. D. Wortmann, J. Koch, M. Reininghaus, C. Unger, C. Hulverscheidt, D.S. Ivanov, B.N. Chichkov, J. Laser Appl. 24, 042017 (2012).
26. D.S. Ivanov, A. Blumenstein, J. Ihlemann, P. Simon, M.E. Garcia, and B. Rethfeld, Appl. Phys. A 123, 744 (2017).
27. R. A. Ganeev, M. Baba, M. Suzuki, and H. Kuroda, J. Modern Opt. 53, 1451 (2006).
28. M. Lewenstein, P. Balcou, M. Y. Ivanov, A. L'Huillier, and P. B. Corkum, Phys. Rev. A 49, 2117 (1994).
29. P. B. Corkum, Phys. Rev. Lett. 71, 1994 (1993).
30. S. Augst, D. Strickland, D. D. Meyerhofer, S. L. Chin, and J. H. Eberly, Phys. Rev. Lett. 63, 2212 (1989).
31. I.J. Kim, C. M. Kim, H. T. Kim, G. H. Lee, Y. S. Lee, J. Y. Park, D. J. Cho, and C. H. Nam, Phys. Rev. Lett. 94, 243901 (2005).
32. J. Mauritsson, P. Johnsson, E. Gustafsson, A. L'Huillier, K. J. Schafer, and M. B. Gaarde, Phys. Rev. Lett. 97, 013001 (2006).
33. J. Kim, G. H. Lee, S. B. Park, Y. S. Lee, T. K. Kim, C. H. Nam, T. Mocek, and K. Jakubczak, Appl. Phys. Lett. 92, 021125 (2008).
34. R. A. Ganeev, V. V. Strelkov, C. Hutchison, A. Zaïr, D. Kilbane, M. A. Khokhlova and J. P. Marangos, Phys. Rev. A 85, 023832 (2012).
35. R. A. Ganeev, C. Hutchison, A. Zaïr, T. Witting, F. Frank, W. A. Okell, J. W. G. Tisch, and J. P. Marangos, Opt. Express 20, 90 (2012).
36. R. A. Ganeev, M. Suzuki, and H. Kuroda, J. Opt. Soc. Am. B 31, 911 (2014).
37. R. A. Ganeev, M. Suzuki, and H. Kuroda, Phys. Rev. A 89, 033821 (2014).
38. R. A. Ganeev, G. S. Boltaev, V. V. Kim, and C. Guo, Nanomater. 9, 572 (2019).
39. J. Seres, V. S. Yakovlev, E. Seres, C. H. Streli, P. Wobrauschek, C. H. Spielmann, and F. Krausz, Nature Phys. 3, 878 (2007).
40. A.Pirri, C. Corsi, and M. Bellini, Phys. Rev. A 78, 011801 (2008).
41. R. A. Ganeev, G. S. Boltaev, V. V. Kim, M. Venkatesh, and C. Guo, OSA Continuum 2, 2381 (2019).
42. R. A. Ganeev, M. Baba, M. Suzuki, and H. Kuroda, Phys. Lett. A 339, 103 (2005).
43. H. Ruf, C. Handschin, R. Cireasa, N. Thiré, A. Ferré, S.Petit, D. Descamps, E. Mével, E. Constant, V. Blanchet, B. Fabre, and Y. Mairesse, Phys. Rev. Lett. 110, 083902 (2013).
44. R. A. Ganeev, M. Suzuki, and H. Kuroda, Eur. Phys. J. D 70, 21 (2016).
45. T. D. Donnelly, T. Ditmire, K. Neuman, M. D. Perry, and R. W. Falcone, Phys. Rev. Lett. 76, 2472 (1996).

46. J. W. G. Tisch, T. Ditmire, D. J. Fraser, N. Hay, M. B. Mason, E. Springate, J. P. Marangos, and M. H. R. Hutchinson, J. Phys. B 30, L709 (1997).
47. C. Vozzi, M. Nisoli, J.-P. Caumes, G. Sansone, S. Stagira, S. De Silvestri, M. Vecchiocattivi, D. Bassi, M. Pascolini, L. Poletto, P. Villoresi, and G. Tondello, Appl. Phys. Lett. 86, 111121 (2005).
48. R. A. Ganeev, M. Suzuki, M. Baba, M. Ichihara, and H. Kuroda, J. Phys. B 41, 045603 (2008).
49. R. A. Ganeev, M. Suzuki, M. Baba, M. Ichihara, and H. Kuroda, J. Opt. Soc. Am. B 25, 325 (2008).
50. R. A. Ganeev, G. S. Boltaev, V. V. Kim, K. Zhang, A. I. Zvyagin, M. S. Smirnov, O. V. Ovchinnikov, P. V. Redkin, M. Wöstmann, H. Zacharias, and C. Guo, Opt. Express 26, 35013 (2018).
51. Y.-Y. Yang, A. Scrinzi, A. Husakou, Q.-G. Li, S. L. Strebbings, F. Süßmann, H.-J. Yu, S. Kim, E. Rühl, J. Herrmann, X. C. Lin, and M. F. Kling, Opt. Express 21, 2195 (2013).
52. G. Vampa, B. G. Ghamsari, S. Siadat Mousavi, T. J. Hammond, A. Olivieri, E. Lisicka-Skrek, E., A. Y. Naumov, D. M. Villeneuve, A. Staudte, P. Berini, and P. B. Corkum, Nature Phys. 13, 659 (2017).
53. P. B. Corkum, F. Brunel, N. K. Sherman, and T. Srinivasan-Rao, Phys. Rev. Lett. 61, 2886 (1988).
54. L. V. Zhigilei, Z. Lin, and D. S. Ivanov, J. Chem. Phys. 113, 11892 (2009).
55. D.S. Ivanov, A.I. Kuznetsov, V.P. Lipp, B. Rethfeld, B.N. Chichkov, M.E. Garcia, W. Schulz, Appl. Phys. A 111, 675 (2013).
56. W.F. Gale and T.C. Totemeier, Smithell's Metal Reference Book, 8th edition, Butterworth-Heinemann, Oxford, (2004).
57. https://www.filmetrics.com
58. D. S. Ivanov and B. C. Rethfeld, Appl. Surf. Sci. 255, 9724 (2009).
59. D. S. Ivanov, V. P. Lipp, V. P. Veiko, E. Jakovlev, B. Rethfeld, and M. E. Garcia, Appl. Phys. A 117, 2133 (2014).
60. L.V. Zhigilei, Z. Lin, and D.S. Ivanov, J. Chem. Phys. 113, 11892 (2009).